Integrated near-field thermophotovoltaic device overcoming blackbody limit

Takuya Inoue,[1,] Keisuke Ikeda,[2] Bongshik Song,[2,3] Taiju Suzuki,[2] Koya Ishino,[2] Takashi Asano,[2] and Susumu Noda[1,2*]*

[1] *Photonics and Electronics Science and Engineering Center, Kyoto University, Kyoto-daigaku-katsura, Nishikyo-ku, Kyoto 615-8510, Japan.*

[2] *Department of Electronic Science and Engineering, Kyoto University, Kyoto-daigaku-katsura, Nishikyo-ku, Kyoto 615-8510, Japan.*

[3] *Department of Electrical and Computer Engineering, Sungkyunkwan University, Suwon 16419, South Korea.*

*t_inoue@qoe.kuee.kyoto-u.ac.jp, snoda@kuee.kyoto-u.ac.jp

ABSTRACT

Near-field thermal radiation transfer overcoming the blackbody limit has attracted significant attention in recent years owing to its potential for drastically increasing the output power and conversion efficiency of thermophotovoltaic (TPV) power generation systems. Here, we experimentally demonstrate a one-chip near-field TPV device overcoming the blackbody limit, which integrates a 20-μm-thick Si emitter and an InGaAs PV cell with a sub-wavelength gap (<140 nm). The device exhibits a photocurrent density of 1.49 A/cm^2 at 1192 K, which is 1.5 times larger than the far-field limit at the same temperature. In addition, we obtain an output power of 1.92 mW and a system efficiency of 0.7% for a 1-mm^2 device, both of which are one to two orders of magnitude greater than those of the previously reported near-field systems. Detailed comparisons between the simulations and experiments reveal the possibility of a system efficiency of >35% in the up-scaled device, thus demonstrating the potential of our integrated near-field TPV device for practical use in the future.

KEYWORDS: thermal emission, near-field thermal radiation transfer, thermophotovoltaics, semiconductor, nanotechnology.

TEXT

Introduction

Thermal radiation transfer between two objects that are separated by a sub-wavelength gap can be orders of magnitude larger than the maximal radiation transfer in free space (the blackbody limit) owing to the contribution of evanescent waves.[1-6] This concept has attracted significant attention in both fundamental science and various energy-related applications in recent years. The thermophotovoltaic (TPV) systems,[7-13] which convert heat into electricity by irradiating PV cells with thermal radiation from heated emitters, can significantly benefit from near-field thermal radiation transfer owing to the potential to increase output power density and conversion efficiency.[14-19] Since the first experimental investigation of near-field TPV systems in 2001,[20] several quantitative demonstrations of near-field TPV systems have been reported in recent years.[21-23] For example, in Ref. 21, an 80-μm-diameter Si thermal emitter and a 300-μm×300-μm mid-infrared photodetector were brought closer to a 60-nm distance using a piezo-controlled experimental setup, and 40-fold enhancement in the output power density was achieved. Another recent work[23] demonstrated a near-field TPV system composed of a 40-μm-diameter graphite emitter and a 20-μm-diameter InSb PV cell cooled at 77 K, where an output power density of 0.75W/cm^2 and a near-field cell conversion efficiency[23] of 14 % were obtained (the detailed configurations and performances of the previous systems[21-23] are provided in Supporting Section 7). However, the generated electrical power in these systems was less than 1–10 μW owing to the small effective device size (<100 μm). In addition, the system efficiency, which is defined by the ratio of the electrical output to the input heating power, was extremely low (<0.01%) owing to the enormous thermal conduction losses of the systems. More importantly, these near-field systems involved external controllers such as

piezoelectric actuators and NEMS actuators for the gap formation, which are not suitable for practical applications. To solve these issues, in our previous study,[24] we developed a near-field TPV device integrating a 2-μm-thick Si emitter with a side length of 500 μm and an InGaAs PV cell, and demonstrated the enhanced photocurrent compared to the corresponding far-field device. The thermal radiation intensity and the generated photocurrent in the above device, however, did not exceed the blackbody limit at the same temperature, and the unintentional contact between the emitter and the PV cell increased the thermal conduction loss, thereby resulting in a relatively low output power (30 μW at 1065 K) and low system efficiency (0.05% at 1065 K).

In this paper, we demonstrate an integrated near-field TPV device that achieves the thermal radiation transfer overcoming the blackbody limit and realize a drastic increase in both the output power and system efficiency. Our one-chip super-Planckian device is based on the realization of a sub-wavelength gap (<140 nm) between a high-temperature emitter (~1200 K) and a room-temperature PV cell without contact over a large area (1 mm^2), which is accomplished by designing a 20-μm-thick Si emitter with supporting beams that can relieve the thermal stress of the emitter while maintaining the mechanical robustness. In addition, an increase of the emitter thickness from 2 to 20 μm facilitates the realization of the near-field thermal radiation transfer beyond the blackbody limit owing to the increase in the photonic density of states. Using this device, we demonstrate a large photocurrent of 14.9 mA (density: 1.49 A/cm^2) at an emitter temperature of 1192 K, which is 1.5 times larger than the blackbody limit at the same temperature. In addition, we obtain an output power of 1.92 mW (density: 0.192 W/cm^2) and a system conversion efficiency of 0.7%, both of which are greater than those of the previously reported near-field TPV systems[21-24] by one to two orders of magnitude. Furthermore, we theoretically predict that a system efficiency of >35% can be achieved in the

up-scaled device with photon recycling, demonstrating the potential of our integrated near-field TPV device in practical applications.

Results

Figure 1(a) shows a bird's eye view and cross section of the proposed device: a 20-μm-thick Si thermal emitter with a side length of 1 mm was integrated on one side of an intermediate Si substrate while maintaining a sub-wavelength gap between them, and a thin InGaAs PV cell of the same size was integrated to the other side of the substrate. We chose undoped Si as an emitter material because it shows smaller absorption coefficients (and weaker thermal radiation intensity) at wavelengths longer than the bandgap of InGaAs ($\lambda > \lambda_{InGaAs}$=1.7 μm) than doped Si, while maintaining large absorption coefficients (strong thermal radiation intensity) at wavelengths shorter than λ_{InGaAs} owing to the interband absorption.[10] In addition, we employed the intermediate undoped Si substrate between the Si emitter and the PV cell to suppress the long-wavelength heat transfer mediated by surface modes at the contact layer of the PV cell[18] (see Supporting Fig. S1 for details). To suspend the millimeter-sized emitter while minimizing the tilt and the thermal conduction loss, we employed 10-μm-width supporting beams at the four corners instead of a single beam employed in our previous study.[24] Because the width of the supporting beams (10 μm) is smaller than the thickness (20 μm), these supporting beams can relieve the thermal stress of the emitter by in-plane deformation, which helps maintain a sub-wavelength gap between the emitter and the PV cell even at high temperatures (see Supporting Section 2 for details). In addition, compared to the thin-film Si thermal emitter (t_e=2 μm),[24] the 20-μm-thick Si thermal emitter enables thermal radiation transfer to overcome the blackbody limit more easily owing to the increase of the photonic density of states inside the emitter (see Supporting Fig. S1 for details). Figure 1(b) shows the calculated thermal radiation transfer spectra from the emitters with two different thicknesses (red line: t_e= 20 μm, blue line: t_e= 2 μm) to the InGaAs PV cell when the emitter temperature

is 1200 K and the gap length is 150 nm. The details of the calculations are explained in Supporting Section 1. By increasing the thickness of the emitter, the radiation intensity below λ_{InGaAs} is enhanced by a factor of 3, which exceeds the blackbody limit (black line) in the entire near-infrared range at the same temperature. The thermal radiation transfer to the PV cell at longer wavelengths is relatively suppressed because the total thickness of the doped layers in the PV cell is only 2.5 μm, which is not sufficient for the doped carriers in the PV cell to induce strong free carrier absorption. It should be noted that the thermal radiation loss in the opposite side of the PV cell (not shown) increases with the emitter thickness but the loss can be reduced by placing the top reflector above the emitter for photon recycling.[19] Figure 1(c) shows the calculated photocurrent density of the PV cell as a function of the gap length; the dashed line shows the calculated photocurrent density for the blackbody spectrum at the same temperature (hereafter, this value is referred to as the blackbody limit of the photocurrent). To obtain a photocurrent density that exceeds the blackbody limit, the gap length should be below 200 nm for the 20-μm-thick emitter, which ensures the tolerance to fabrication errors compared to that required for the 2-μm-thick emitter (below 100 nm).

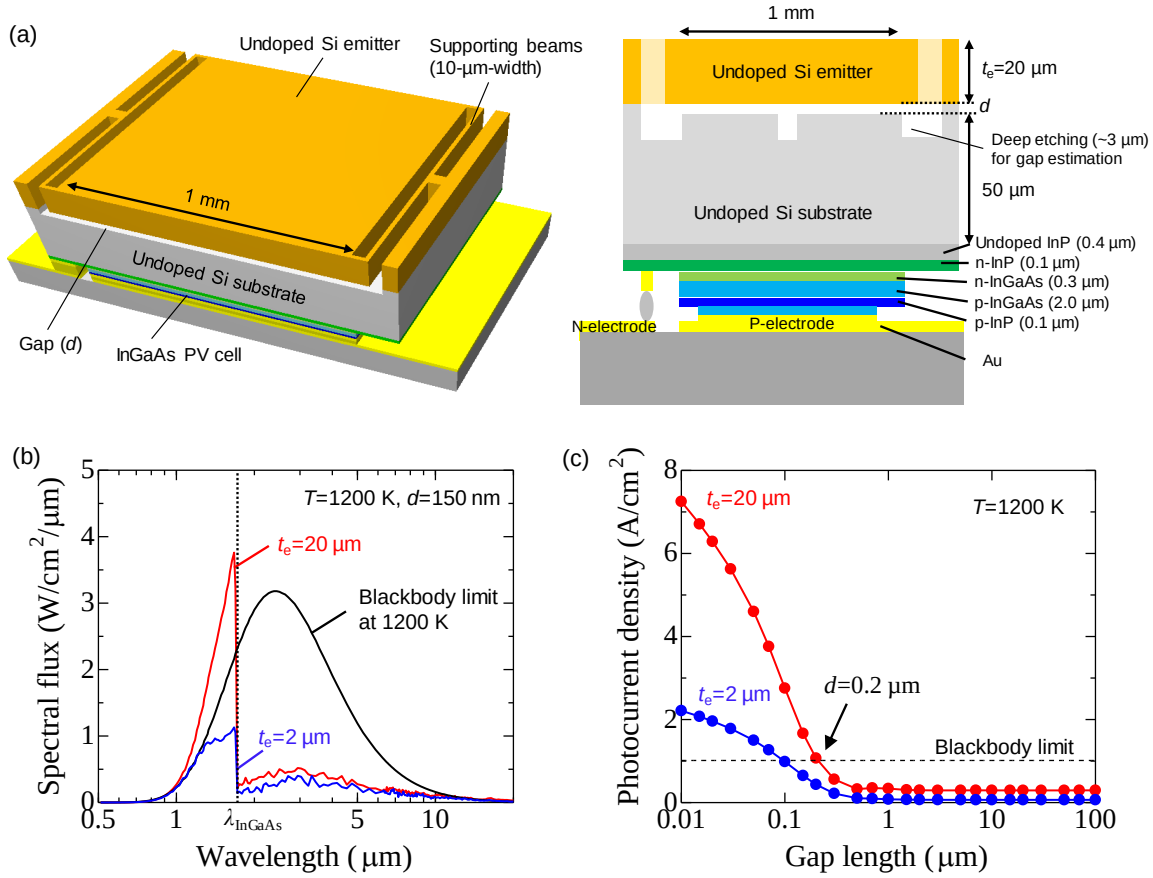

Fig. 1. Schematics and calculated performances. (a) Bird's eye view and cross section of near-field TPV device integrating 20-μm-thick Si thermal emitter and InGaAs PV cell. (b) Calculated thermal radiation transfer spectrum to the InGaAs PV cell for a 20-μm-thick (red) and 2-μm-thick (blue) Si thermal emitter when the gap length is 150 nm and the emitter temperature of 1200 K. Black line shows the blackbody spectrum at 1200 K. (c) Calculated photocurrent density of the near-field TPV device with a 20-μm-thick (red) and 2-μm-thick (blue) Si thermal emitter at 1200 K. Dashed line shows the calculated photocurrent density for the blackbody spectrum at the same temperature (blackbody limit).

Figure 2(a) shows a microscope image of the fabricated Si thermal emitter with a side length of 1 mm, which was integrated on top of the intermediate Si substrate via Si-Si bonding[25]

(the details of the fabrication process are explained in Methods and Supporting Fig. S3). The gap length d was controlled by the surface etching of the intermediate substrate before chip-to-chip bonding. Here, we fabricated one far-field TPV device (Device I, d~2900 nm) and two near-field TPV devices (Device II and III, d~150 nm), wherein the latter devices contain a small portion of 2900-nm-deep trenches with a side length of 0.1 mm for gap estimation. The microscope image of the fabricated 10-μm-width supporting beam is shown in the right panel. Because of the relatively strong mechanical strength of the 20-μm-thick Si slab, we can maintain the flatness of the emitter even with such elongated supporting beams. Figure 2(b) shows the microscope images of the fabricated InGaAs PV cells with a side length of 1 mm, which were integrated at the bottom of the intermediate substrate via plasma-assisted wafer bonding.[26] In this work, we investigated two types of PV cells; one (left panel, employed in Device I and II) has a comb-like p-type electrode (Au), while the other (right panel, employed in Device III) has a uniform p-type electrode. The comb-like electrode can reduce the absorption of sub-bandgap photons at the interface between the Au and the semiconductor, and thus, it is potentially suitable for high-efficiency TPV systems, but it leads to a higher series resistance of the PV cell owing to the low electrical conductance of the p-type semiconductor layer.

Before the near-field TPV experiment, we measured the in-plane distribution of the gap length of the fabricated three devices by varying the heating power of the Si emitter (see Methods). In this work, the heating of the emitter was performed by laser irradiation for the purpose of the proof-of-concept demonstration, while it can be replaced with another heat source such as concentrated sunlight irradiation in the future. We measured the reflection spectra at 5 × 5 points in each device by irradiating it with a broadband infrared light and estimated the gap length and the emitter temperature at each point from the Fabry-Perot interference of the device (the detailed procedure for the gap and temperature measurement is

provided in Methods and Supporting Section 4). Figure 2(c) shows the temperature dependence of the obtained gap lengths of the three devices, wherein the maximum, average, and minimum gap lengths within each device are shown in red, black, and blue, respectively. Although the obtained gap length was not uniform for each device [Fig. 2(c) and Supporting Fig. S4], the average gap length of each device remains almost the same for a wide range of emitter temperatures (300–1200 K). Among the three devices, Device II has the smallest average gap length (<140 nm at the emitter temperature of 1192 K), which satisfies the condition for exceeding the blackbody limit shown in Fig. 1(c).

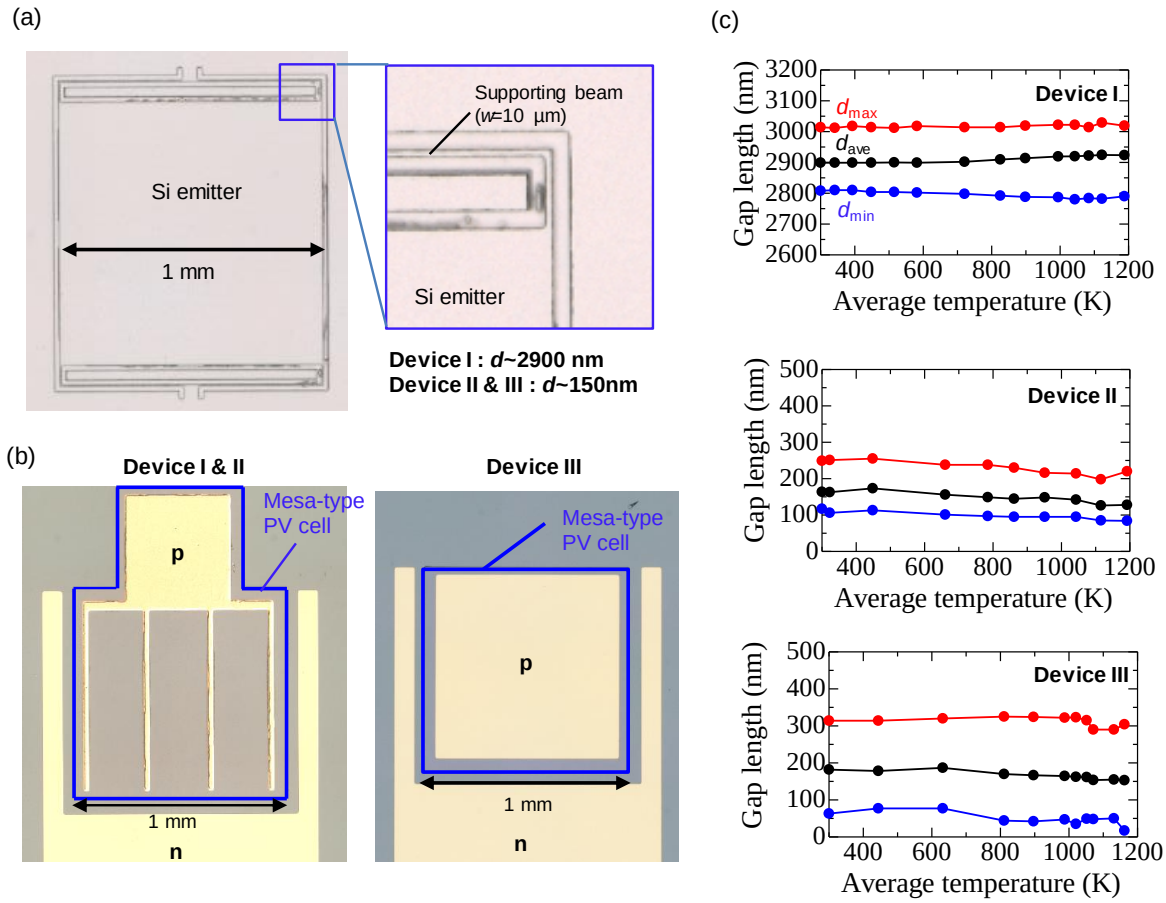

Fig. 2. Fabricated devices. (a) Microscope image of the fabricated Si emitter and enlarged view of the supporting beam. (b) Microscope image of the fabricated InGaAs PV cells with a comb-like p-type electrode (left) and a uniform p-type electrode (right). (c) Measured gap

lengths of the fabricated three near-field TPV devices as a function of the average temperature of the emitter.

Figures 3(a) and 3(b) show the measured current-voltage (I-V) characteristics of the far-field TPV device (Device I, d_{ave}~2900 nm) and the near-field TPV device (Device II, d_{ave}~140 nm) for various emitter temperatures. It should be noted that both devices contain an emitter and a PV cell with the same structures, and the only difference is the average gap length. Here, Device II yields much larger photocurrents than Device I. For example, at the same emitter temperature of 1043 K, Device II yields a short-circuit current (2.69 mA) that is 7.3 times larger than that of Device I (0.37 mA). It should be noted that in Device II, the short-circuit currents at 0 V at higher emitter temperatures (1116 and 1192 K) were less than the original photocurrents generated by the near-field thermal radiation transfer owing to the series resistance of the PV cell. Because the photocurrent densities in Device II are much higher than those of the typical solar cells, even a small series resistance induces a non-negligible internal forward bias on the p-n junction, and thus, a part of the generated photocurrent is internally consumed as a forward current (see Supporting Section 5). Therefore, the original photocurrent generated by the near-field thermal radiation transfer can be accurately measured by applying a sufficient reverse bias to cancel this internal forward bias. Figure 3(c) shows the measured and calculated photocurrent densities of the two devices at a reverse bias of −1 V as a function of the average emitter temperature. The measured photocurrent densities of the fabricated devices (red and blue triangles) agree well with the calculated ones (red and blue dashed lines). More importantly, the obtained photocurrent density in Device II exceeds the blackbody limit (black solid line) at an emitter temperature larger than 1050 K; for example, the obtained photocurrent density at 1192 K is 1.49 A/cm^2, which is 1.5 times larger than the blackbody limit at the same temperature (0.96 A/cm^2). This result is supported by the calculated near-field

thermal radiation transfer spectrum shown in Fig. 3(d), wherein the spectral flux absorbed in the p-n junction exceeds the blackbody limit (black line) in the entire near-infrared range below the bandgap wavelength of InGaAs (λ_{InGaAs}=1.7 μm).

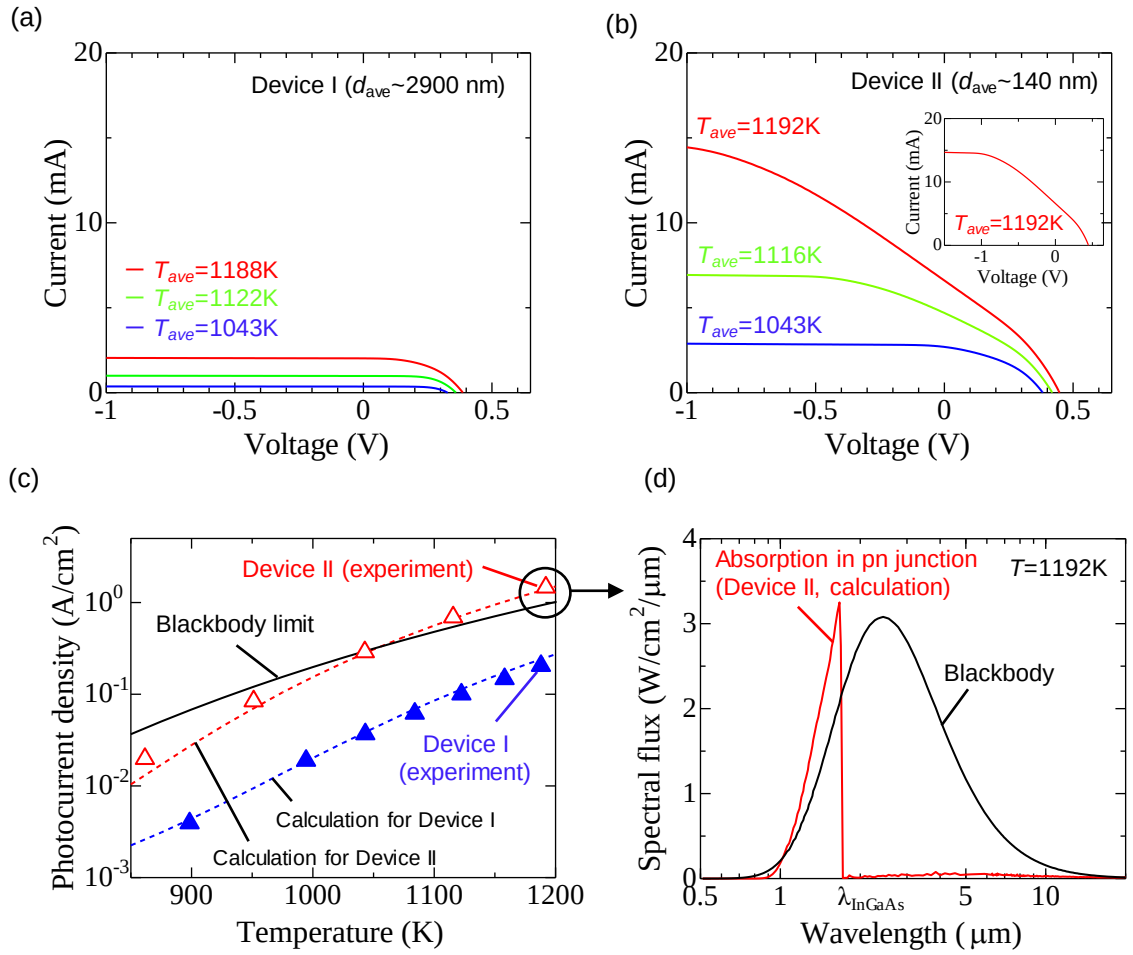

Fig. 3. Photocurrent generation overcoming blackbody limit. (a) Measured current-voltage characteristics of the far-field TPV device (Device I) at three different emitter temperatures. (b) Measured current-voltage characteristics of the near-field TPV device (Device II) at three different emitter temperatures. As shown in the inset, the original photocurrent generated by the near-field thermal radiation transfer can be accurately measured by applying a sufficient reverse bias. (c) Measured (triangles) and calculated (dashed lines) photocurrent density of the two devices as a function of the average emitter temperature. Gap lengths of 3000 nm and 150

nm (except for deep trenches) were assumed in the calculations for Device I and Device II, respectively. Black solid line shows the calculated blackbody limit for the InGaAs PV cell. (d) Calculated near-field thermal radiation transfer spectrum from the emitter to the p-n junction of the PV cell for Device II at 1192 K, wherein the gap length of 150 nm was assumed except for deep trenches.

Finally, we evaluated the actual system efficiency of our near-field TPV system by measuring both the input heating power of the emitter and the electrical output power. In this experiment, we characterized Device III, which has the lowest series resistance of the PV cell owing to the employment of the uniform p-type electrode [shown in the right panel of Fig. 2(b)]. The black dots in Fig. 4(a) show the relationship between the heating power of the emitter and the average temperature of the emitter in Device III. The black dashed line shows the calculated heat conduction loss through the supporting beams based on the temperature dependence of the thermal conductivity of Si.[27] When the temperature is lower than 650 K, the heating power of the emitter can be evaluated with the calculated heat conduction loss. The required heating power at higher temperatures exceeds the calculated conduction loss owing to the non-linear increase of the near-field thermal radiation power. The dashed lines (blue and red) show the calculation results obtained by taking the sum of the thermal conduction loss and the calculated total thermal radiation power from the emitter. Here, we varied the effective reflectance of the bottom electrode (R_{bottom}) to take into account the in-plane loss of thermal radiation in the finite-size device, where a portion of the waves reflected at the bottom electrode cannot return to the emitter (see Supporting Section 6). The experimental results agree well with the calculations with R_{bottom} =0.66, which is lower than the reflectance of the ideal Au reflector (R_{Au}=0.96). Figure 4(b) shows the measured I-V characteristics of Device III (solid line) and Device II (dashed line) at almost the same heating power, wherein Device III yields

a much larger electrical output power owing to the smaller series resistance of the PV cell. Figure 4(c) shows the electrical output power density and system efficiency of Device III as a function of the emitter temperature. At an emitter temperature of 1162 K, we obtain the electrical power density of 0.192 W/cm^2. Although the obtained power density is smaller than the highest value ever reported (0.75W/cm^2),[23] the absolute value of the electrical output power (1.92 mW) is two orders of magnitude larger than those of the previously demonstrated near-field TPV devices[21-24] owing to the larger device size (1 mm^2) and the higher emitter temperature. The maximum system efficiency of our device is 0.7 %, which is one order of magnitude higher than that of our previous near-field TPV device (0.05%).[24] It should also be noted that the other previous demonstrations of near-field TPV systems[21-23] did not focus on the reduction of the thermal conduction loss from the emitter and resulted in lower system efficiencies (<0.01%). More detailed comparisons of the TPV performance such as the cell conversion efficiency excluding the thermal conduction loss are provided in Supporting Section 7.

To increase the system efficiency, we should further decrease the gap length and increase the emitter temperature to enhance the near-field thermal radiation transfer below the bandgap wavelength of the PV cell. Figure 4(d) shows the calculated efficiency of the ideal near-field TPV devices with three gap lengths as a function of the emitter temperature. In this calculation, we assumed an infinite-size device with no conduction loss and ideal bottom reflectors (R_{bottom}=R_{Au}=0.96). We also modeled the dark current of the InGaAs PV cell by fitting the measured I-V characteristics (see Supporting Section 5) and neglected the series resistance for the ideal case. The solid lines show the efficiency of the device without a top Au reflector above the emitter as shown in Fig. 1(a), while the dashed lines show the efficiency of the device with a top Au reflector for photon recycling.[19] As seen in the figure, we can obtain the efficiency of ~20% without photon recycling by reducing the gap length to 75 nm at the

temperatures higher than 1300 K. In addition, a higher conversion efficiency (>35%) can be achieved by placing the top Au reflector above the emitter and by recycling the thermal radiation opposite to the PV cell.

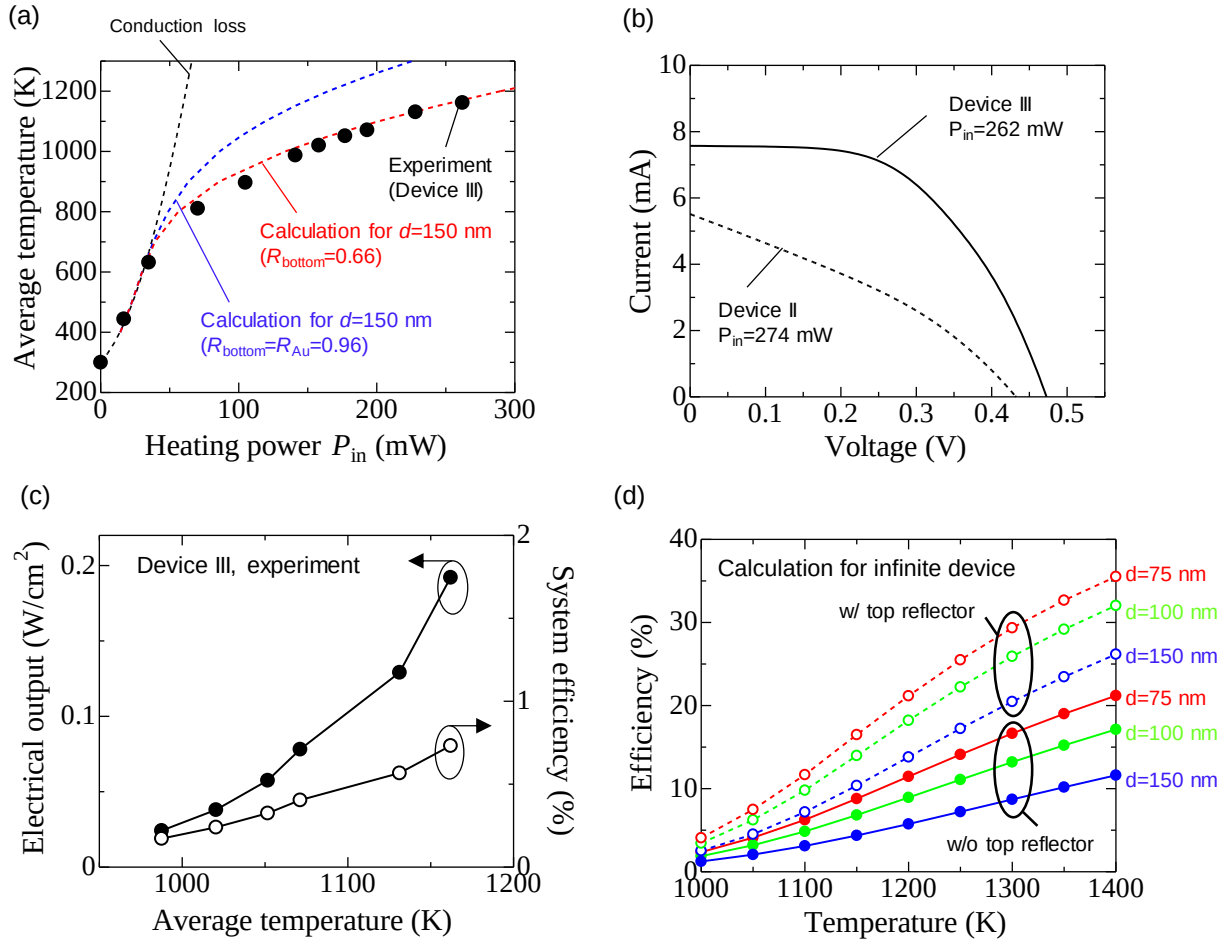

Fig. 4. System efficiency of fabricated device and ideal device. (a) Relationship between the heating power of the emitter (P_{in}) and the average temperature of the emitter in Device III. Black dashed line shows the calculated conduction loss of the emitter. Blue and red dashed lines show the calculation results obtained by taking the sum of thermal conduction loss and total thermal radiation power from the emitter, wherein we varied the effective reflectance of the bottom electrode (R_{bottom}). (b) Measured I-V characteristic of Device III at P_{in}=262 mW (solid line). I-V characteristic of Device II at almost the same P_{in} is shown with a dashed line for comparison. (c) Measured output power density and system efficiency of Device III as a

function of the emitter temperature. (d) Calculated system efficiency of an infinite-size near-field TPV device (R_{bottom}=R_{Au}, no conduction loss) with various gap lengths as a function of the emitter temperature. Solid and dashed lines show the efficiency of the system without and with a top Au reflector (R_{top}=R_{Au}) for photon recycling. In this calculation, we neglected the series resistance of the PV cell for ideal case.

Discussion

To experimentally realize the ideal system efficiencies shown in Fig. 4(d), several improvements in the device structure are necessary. First, we should further reduce the thermal conduction loss [black dashed line in Fig. 4(a)] and the additional thermal radiation loss due to the non-unity bottom reflectivity R_{bottom} [shown with the power difference between the blue and red dashed lines in Fig. 4(a)]. Because these two losses stem from the finiteness of the device size, we can decrease them by scaling up the device size. Second, we should reduce the series resistance of the PV cell by optimizing the doping density of the n-doped contact layers to improve the fill factor of the I-V characteristics of the fabricated PV cell. Finally, to realize a smaller gap length at higher emitter temperatures, we should optimize the supporting structures of the emitter to further suppress the tilting and bowing of the emitter during heating.

In summary, we have developed a near-field TPV device integrating a 20-μm thick Si emitter and an InGaAs PV cell with a sub-wavelength gap (< 140 nm) without contact over a large area (1 mm^2). Using this device, we have demonstrated a large photocurrent (density) of 14.9 mA (1.49 A/cm^2) at 1192 K, which exceeds the blackbody limit at the same temperature. In addition, by measuring both the input heating power and the electrical output power of our near-field TPV devices, we have obtained an output power of 1.92 mW and a system efficiency of 0.7%. We have also revealed that a high system efficiency (>35%) can be achieved in an up-scaled device by placing a top reflector above the emitter for photon recycling. Our one-chip super-Planckian devices will contribute to the full exploitation of near-field thermal

radiation transfer in various applications including solar thermophotovoltaics and waste heat recovery.

Methods

Sample preparation: We prepared an SOI substrate with a 20-μm-thick top Si layer and a 1-μm-thick SiO_2 layer on a 650-μm-thick Si substrate (SOI-A) for the Si emitter, and another SOI substrate with a 50-μm-thick top Si layer and a 1-μm-thick SiO_2 layer on a 300-μm-thick Si substrate (SOI-B) for the intermediate Si substrate. The epitaxial wafer for InGaAs PV cells consisted of 400-nm undoped-InP/100-nm n-InP ($n_d = 2 \times 10^{18}$ cm^{-3})/300-nm n-$In_{0.53}Ga_{0.47}As$ ($n_d = 1 \times 10^{18}$ cm^{-3})/2000-nm p-$In_{0.53}Ga_{0.47}As$ ($n_a = 1 \times 10^{17}$ cm^{-3})/100-nm p-InP ($n_a = 2 \times 10^{18}$ cm^{-3})/300-nm p- $In_{0.53}Ga_{0.47}As$ ($n_a = 2 \times 10^{18}$ cm^{-3})/350-μm InP substrate. We first fabricated a Si emitter (1 × 1 mm) with four L-shaped supporting beams (width:10 μm, length:580 μm) on SOI-A by electron-beam (EB) lithography and cryogenic reactive ion etching (RIE). Next, we created a trench (Device I: 2900 nm, Device II and III: 150 nm) on SOI-B by RIE, in order to leave the gap between the emitter and the PV cell in the subsequent bonding process. For Devices II and III, we also created nine deeper trenches (~2900 nm) with a side length of 100 μm for gap estimation. After hydrophilizing the surfaces of the two substrates, we bonded them using a high-precision alignment and bonding system. The bonded sample was heated to 473 K in vacuum for 1 h and at 1273 K in Ar atmosphere for 1 h to increase the bonding strength. The upper Si substrate and SiO_2 layer were then removed by RIE and HF solution, respectively, to bare the 50-μm-thick intermediate Si substrate. The bonding of the intermediate Si substrate and the epi-structure for the PV cell was performed by oxygen plasma activation and 1-h post-annealing at 423 K in vacuum. The InP substrate was removed with HCl solution, and a mesa-type PV cell structure was formed by photolithography, metal deposition, and a lift-off process. The fabricated PV cell was then fixed on a supporting insulating substrate (Au/Ti/SiO_2/Si) by flip-chip bonding using a conductive adhesive (Ag paste). Finally, the Si substrate and SiO_2

layer above the emitter were removed by RIE and vapor HF etching, respectively, to bare the 20-μm-thick Si emitter. The schematic of each fabrication process is shown in Supporting Fig. S3.

Experimental procedures: The Si emitters were heated by irradiation with a green laser (λ=532 nm) in a vacuum chamber (<1×10^{-3} Pa). The heating power of the device, P_{in}, was calculated by considering the incident laser power and the theoretical reflectivity of Si at elevated temperatures. It should be noted that no laser light penetrates the emitter owing to sufficient absorption inside the 20-μm-thick emitter. To measure the emitter temperature and the gap length between the emitter and the intermediate substrate, we irradiated the device with broadband infrared light (wavelength range: 1000–1650 nm) and measured the reflection spectra for 5 × 5 points at 225-μm intervals in each device with a near-infrared spectrometer (Ocean Photonics, NIRQuest512). We then estimated the gap length and the emitter temperature at each point from the resonant wavelengths of the Fabry-Perot interference of the device (the details are explained in Supporting Section 4). The current-voltage characteristics of the PV cells were measured with a precision source/measure unit (Keysight, B2901A). The temperatures of the PV cells were kept at room temperature without any cooling system. During the experiment, we monitored the temperature of the stainless base to which the PV cell was attached and confirmed that the temperature increase of the base was smaller than 1 K at the maximum heating power (~300 mW).

AUTHOR INFORMATION

Corresponding Authors

*E-mail: t_inoue@qoe.kuee.kyoto-u.ac.jp, snoda@kuee.kyoto-u.ac.jp

Author Contributions

TI, TA, and SN supervised the entire project. TI designed and fabricated samples with KI and BS. KI performed the experiments and analyzed the data with TI, ST, and KI. All the authors discussed the results and wrote the manuscript. All authors have given approval to the final version of the manuscript.

Competing Interests

Authors declare that they have no competing interests.

ACKNOWLEDGMENT

This work was partially supported by a Grant-in-Aid for Scientific Research (17H06125) from the Japan Society for the Promotion of Science (JSPS).

ASSOCIATED CONTENT

Supporting Information

Supporting Information Available: (1) Simulation of near-field thermal radiation transfer. (2) Simulation of temperature distribution and vertical displacement of emitter. (3) Fabrication of near-field TPV device. (4) Estimation of emitter temperature and gap size of fabricated devices. (5) Theoretical modeling of PV cell. (6) Effective bottom reflectivity in finite-size device. (7) Detailed comparison of TPV performances between this work and previous works. This material is available free of charge via the Internet at http://pubs.acs.org.

REFERENCES

(1) Polder, D.; Hove, M. V. Theory of radiative heat transfer between closely spaced bodies. *Phys*. *Rev*. *B* **1971**, *4*, 3303–3314.

(2) Ottens, R. S.; Quetschke, V.; Wise, S.; Alemi, A. A.; Lundock, R.; Mueller, G.; Reitze, D. H.; Tanner, D. B.; Whiting, B. F. Near-Field Radiative Heat Transfer between Macroscopic Planar Surfaces. *Phys*. *Rev*. *Lett*. **2011**, *107*, 014301.

(3) Song, B.; Ganjeh, Y.; Sadat, S.; Thompson, D.; Fiorino, A.; Fernandez-Hurtado, V.; Feist, J.; Garcia-Vidal, F. J.; Cuevas, J. C.; Reddy, P.; Meyhofer, E. Enhancement of near-field radiative heat transfer using polar dielectric thin films. *Nat*. *Nanotechnol*. **2015**, *10*, 253–258.

(4) St-Gelais, R.; Zhu, L.; Fan, S.; Lipson, M. Near-field radiative heat transfer between parallel structures in the deep subwavelength regime. *Nat. Nanotechnol*. **2016**, *11*, 515–520.

(5) DeSutter, J.; Tang, L.; Francoeur, M. A near-field radiative heat transfer device. *Nat*. *Nanotechnol*. **2019**, *14*, 751–755.

(6) Salihoglu, H.; Nam, W.; Traverso, L.; Segovia, M.; Venuthurumilli, P. K.; Liu, W.; Wei, Y.; Li, W.; Xu, X. Near-field thermal radiation between two plates with sub-10 nm vacuum separation. *Nano Lett*. **2020**, *20*, 6091–6096.

(7) Swanson, R. M. A proposed thermophotovoltaic solar energy conversion system. *Proc*. *IEEE* **1979**, *67*, 446–447.

(8) Shimizu, M.; Kohiyama, A.; Yugami, H. High-efficiency solar-thermophotovoltaic system equipped with a monolithic planar selective absorber/emitter. *J*. *Photonics Energy* **2015**, *5*, 053099.

(9) Bierman, D. M.; Lenert, A.; Chan, W. R.; Bhatia, B.; Celanović, I.; Soljačić, M.; Wang, E. N. Enhanced photovoltaic energy conversion using thermally-based spectral shaping. *Nat*. *Energy* **2016**, *1*, 16068.

(10) Asano, T.; Suemitsu, M.; Hashimoto, K.; Zoysa, M. De; Shibahara, T.; Tsutsumi, T.; Noda, S. Near-infrared–to–visible highly selective thermal emitters based on an intrinsic semiconductor. *Sci*. *Adv*. **2016**, *2*, e1600499.

(11) Omair, Z.; Scranton, G.; Pazos-Outón, L. M.; Xiao, T. P.; Steiner, M. A.; Ganapati, V.; Peterson, P. F.; Holzrichter, J.; Atwater, H.; Yablonovitch, E. Ultraefficient thermophotovoltaic power conversion by band-edge spectral filtering. *Proc*. *Natl*. *Acad*. *Sci*. *USA* **2019**, *116*, 15356−15361.

(12) Fan, D.; Burger, T.; McSherry, S.; Lee, B.; Lenert, A.; Forrest, S. R. Near-perfect photon utilization in an air-bridge thermophotovoltaic cell. *Nature* **2020**, *586*, 237–241.

(13) Suemitsu, M.; Asano, T.; Inoue, T.; Noda, S. High-efficiency thermophotovoltaic system that employs an emitter based on a silicon rod-type photonic crystal. *ACS Photonics* **2020**, *7*, 80−87.

(14) Laroche, M.; Carminati, R.; Greffet, J.-J. Near-field thermophotovoltaic energy conversion. *J*. *Appl*. *Phys*. **2006**, *100*, 063704.

(15) Ilic, O.; Jablan, M.; Joannopoulos, J. D.; Celanovic, I.; Soljačić, M. Overcoming the black body limit in plasmonic and graphene near-field thermophotovoltaic systems. *Opt*. *Express* **2012**, *20*, A367–A384.

(16) Tong, J. K.; Hsu, W.-C.; Huang, Y.; Boriskina, S. V.; Chen, G. Thin-film 'thermal well' emitters and absorbers for high-efficiency thermophotovoltaics. *Sci*. *Rep*. **2015**, *5*, 10661.

(17) Bernardi, M. P.; Dupré, O.; Blandre, E.; Chapuis, P.-O.; Vaillon, R. Francoeur, M. Impacts of propagating, frustrated and surface modes on radiative, electrical and thermal losses in nanoscale-gap thermophotovoltaic power generators. *Sci*. *Rep*. **2015**, *5*, 11626.

(18) Inoue, T.; Watanabe, K.; Asano, T.; Noda, S. Near-field thermophotovoltaic energy conversion using an intermediate transparent substrate. *Opt*. *Express* **2018**, *26*, A192–A208.

(19) Inoue, T.; Suzuki, T.; Ikeda, K.; Asano, T.; Noda, S. Near-field thermophotovoltaic devices with surrounding non-contact reflectors for efficient photon recycling. *Opt*. *Express* **2021**, *29*, 11133–11143.

(20) DiMatteo, R.; Greiff, P.; Finberg, S. L.; Young-Waithe, K. A.; Choy, H. K. H.; Masaki, M. M.; Fonstad, C. G. Enhanced photogeneration of carriers in a semiconductor via coupling across a nonisothermal nanoscale vacuum gap. *Appl*. *Phys*. *Lett*. **2001**, *79*, 1894–1896.

(21) Fiorino, A.; Zhu, L.; Thompson, D.; Mittapally, R.; Reddy, P.; Meyhofer, E. Nanogap near-field thermophotovoltaics. *Nat*. *Nanotechnol*. **2018**, *13*, 806–811.

(22) Bhatt, G. R.; Zhao, B.; Roberts, S.; Datta, I.; Mohanty, A.; Lin, T.; Hartmann, J.-M.; St-Gelais, R.; Fan, S.; Lipson, M. Integrated near-field thermo-photovoltaics for heat recycling. *Nat*. *Commun*. **2020**, *11*, 2545.

(23) Lucchesi, C.; Cakiroglu, D.; Perez, J.-P.; Taliercio, T.; Tournié, E.; Chapuis, P.-O.; Vaillon, R. Near-Field thermophotovoltaic conversion with high electrical power density and cell efficiency above 14%. *Nano Lett.* **2021**, *21*, 4524–4529.

(24) Inoue, T.; Koyama, T.; Kang, D. D.; Ikeda, K.; Asano, T.; Noda, S. One-chip near-field thermophotovoltaic device integrating a thin-film thermal emitter and photovoltaic cell. *Nano Lett*. **2019**, *19*, 3948–3952.

(25) Kawashima, S.; Imada, M.; Ishizaki, K.; Noda, S. High-precision alignment and bonding system for the fabrication of 3-D nanostructures. *J. Microelectromech. Syst.* **2007**, *16*, 1140–1144.

(26) Pasquariello, D.; Hjort, K. Plasma-assisted InP-to-Si low temperature wafer bondings. *IEEE J. Sel. Top. Quantum Electron.* **2002**, *8*, 118–131.

(27) Shanks, H. R.; Maycock, P. D.; Sidles, P. H.; Danielson, G. C. Thermal conductivity of silicon from 300 to 1400K. *Phys. Rev.* **1963**, *130*, 1743–1748.